

# Airway compliance measured by anatomic optical coherence tomography

RUOFEI BU,<sup>1</sup> SANTOSH BALAKRISHNAN,<sup>1</sup> NICUSOR IFTIMIA,<sup>2</sup> HILLEL PRICE,<sup>3</sup> CARLTON ZDANSKI,<sup>4</sup> AND AMY L. OLDENBURG<sup>1,3,5,\*</sup>

<sup>1</sup>Department of Biomedical Engineering, University of North Carolina at Chapel Hill, Chapel Hill, NC 27599-3216, USA

<sup>2</sup>Physical Sciences Inc., New England Business Center, Andover, MA 01810, USA

<sup>3</sup>Department of Physics and Astronomy, University of North Carolina at Chapel Hill, Chapel Hill, NC 27599-3255, USA

<sup>4</sup>Department of Otolaryngology/Head and Neck Surgery, University of North Carolina at Chapel Hill, Chapel Hill, NC 27599-7070, USA

<sup>5</sup>Biomedical Research Imaging Center, University of North Carolina at Chapel Hill, Chapel Hill, NC 27514, USA

\*aold@physics.unc.edu

**Abstract:** Quantification of airway compliance can aid in the diagnosis and treatment of obstructive airway disorders by detecting regions vulnerable to collapse. Here we evaluate the ability of a swept-source anatomic optical coherence tomography (SSaOCT) system to quantify airway cross-sectional compliance (CC) by measuring changes in the luminal cross-sectional area (CSA) under physiologically relevant pressures of 10–40 cmH<sub>2</sub>O. The accuracy and precision of CC measurements are determined using simulations of non-uniform rotation distortion (NURD) endemic to endoscopic scanning, and experiments performed in a simplified tube phantom and *ex vivo* porcine tracheas. NURD simulations show that CC measurements are typically more accurate than that of the CSAs from which they are derived. Phantom measurements of CSA versus pressure exhibit high linearity ( $R^2 > 0.99$ ), validating the dynamic range of the SSaOCT system. Tracheas also exhibited high linearity ( $R^2 = 0.98$ ) suggestive of linear elasticity, while CC measurements were obtained with typically  $\pm 12\%$  standard error.

© 2017 Optical Society of America

**OCIS codes:** (110.4500) Optical coherence tomography; (170.3880) Medical and biological imaging; (170.3890) Medical optics instrumentation; (170.2150) Endoscopic imaging.

## References and links

1. T. Young, P. E. Peppard, and D. J. Gottlieb, "Epidemiology of Obstructive Sleep Apnea: a population health perspective," *Am. J. Respir. Crit. Care Med.* **165**(9), 1217–1239 (2002).
2. I. C. Gleadhill, A. R. Schwartz, N. Schubert, R. A. Wise, S. Permutt, and P. L. Smith, "Upper airway collapsibility in snorers and in patients with obstructive hypopnea and apnea," *Am. Rev. Respir. Dis.* **143**(6), 1300–1303 (1991).
3. S. D. Murgu and H. G. Colt, "Tracheobronchomalacia and excessive dynamic airway collapse," *Respirology* **11**(4), 388–406 (2006).
4. J. Mead, "Contribution of compliance of airways to frequency-dependent behavior of lungs," *J. Appl. Physiol.* **26**(5), 670–673 (1969).
5. S. T. Kuna, D. G. Bedi, and C. Ryckman, "Effect of Nasal Airway Positive Pressure on Upper Airway Size and Configuration," *Am. Rev. Respir. Dis.* **138**(4), 969–975 (1988).
6. J. A. Rowley, C. S. Sanders, B. R. Zahn, and M. S. Badr, "Gender differences in upper airway compliance during NREM sleep: role of neck circumference," *J. Appl. Physiol.* **92**(6), 2535–2541 (2002).
7. S. C. Persak, S. Sin, J. M. McDonough, R. Arens, and D. M. Wootton, "Noninvasive estimation of pharyngeal airway resistance and compliance in children based on volume-gated dynamic MRI and computational fluid dynamics," *J. Appl. Physiol.* **111**(6), 1819–1827 (2011).
8. D. J. Brenner and E. J. Hall, "Computed tomography--an increasing source of radiation exposure," *N. Engl. J. Med.* **357**(22), 2277–2284 (2007).
9. D. Huang, E. A. Swanson, C. P. Lin, J. S. Schuman, W. G. Stinson, W. Chang, M. R. Hee, T. Flotte, K. Gregory, C. A. Puliafito, and J. G. Fujimoto, "Optical coherence tomography," *Science* **254**(5035), 1178–1181 (1991).
10. J. Schmitt, "OCT elastography: imaging microscopic deformation and strain of tissue," *Opt. Express* **3**(6), 199–

- 211 (1998).
11. J. Armstrong, M. Leigh, I. Walton, A. Zvyagin, S. Alexandrov, S. Schwer, D. Sampson, D. Hillman, and P. Eastwood, "In vivo size and shape measurement of the human upper airway using endoscopic longrange optical coherence tomography," *Opt. Express* **11**(15), 1817–1826 (2003).
  12. J. Jing, J. Zhang, A. C. Loy, B. J. F. Wong, and Z. Chen, "High-speed upper-airway imaging using full-range optical coherence tomography," *J. Biomed. Opt.* **17**(11), 110507 (2012).
  13. M. Choma, M. Sarunic, C. Yang, and J. Izatt, "Sensitivity advantage of swept source and Fourier domain optical coherence tomography," *Opt. Express* **11**(18), 2183–2189 (2003).
  14. J. H. Walsh, M. S. Leigh, A. Paduch, K. J. Maddison, D. L. Philippe, J. J. Armstrong, D. D. Sampson, D. R. Hillman, and P. R. Eastwood, "Evaluation of pharyngeal shape and size using anatomical optical coherence tomography in individuals with and without obstructive sleep apnoea," *J. Sleep Res.* **17**(2), 230–238 (2008).
  15. J. Cisonni, A. D. Lucey, J. H. Walsh, A. J. C. King, N. S. J. Elliott, D. D. Sampson, P. R. Eastwood, and D. R. Hillman, "Effect of the velopharynx on intraluminal pressures in reconstructed pharynges derived from individuals with and without sleep apnea," *J. Biomech.* **46**(14), 2504–2512 (2013).
  16. J. J. Armstrong, M. S. Leigh, D. D. Sampson, J. H. Walsh, D. R. Hillman, and P. R. Eastwood, "Quantitative upper airway imaging with anatomic optical coherence tomography," *Am. J. Respir. Crit. Care Med.* **173**(2), 226–233 (2006).
  17. J. P. Williamson, R. A. McLaughlin, W. J. Noffsinger, A. L. James, V. A. Baker, A. Curatolo, J. J. Armstrong, A. Regli, K. L. Shepherd, G. B. Marks, D. D. Sampson, D. R. Hillman, and P. R. Eastwood, "Elastic properties of the central airways in obstructive lung diseases measured using anatomical optical coherence tomography," *Am. J. Respir. Crit. Care Med.* **183**(5), 612–619 (2011).
  18. G. K. Sharma, A. Chin Loy, E. Su, J. Jing, Z. Chen, B. J.-F. Wong, and S. Verma, "Quantitative Evaluation of Adult Subglottic Stenosis Using Intraoperative Long-range Optical Coherence Tomography," *Ann. Otol. Rhinol. Laryngol.* **125**(10), 815–822 (2016).
  19. K. Wijesundara, C. Zdanski, J. Kimbell, H. Price, N. Ifimia, and A. L. Oldenburg, "Quantitative upper airway endoscopy with swept-source anatomical optical coherence tomography," *Biomed. Opt. Express* **5**(3), 788–799 (2014).
  20. Y. Kawase, Y. Suzuki, F. Ikeno, R. Yoneyama, K. Hoshino, H. Q. Ly, G. T. Lau, M. Hayase, A. C. Yeung, R. J. Hajjar, and I.-K. Jang, "Comparison of nonuniform rotational distortion between mechanical IVUS and OCT using a phantom model," *Ultrasound Med. Biol.* **33**(1), 67–73 (2007).
  21. R. Bu, H. Price, S. Mitran, C. Zdanski, and A. L. Oldenburg, "Swept-source anatomic optical coherence elastography of porcine trachea," *Proc SPIE Int Soc Opt Eng* **9689**, 968923 (2016).
  22. S. P. Timoshenko and J. N. Goodier, "Theory of elasticity," *Eng. Soc. Monogr.* **7**, 806 (1970).
  23. C. W. Bollen, G. T. J. van Well, T. Sherry, R. J. Beale, S. Shah, G. Findlay, M. Monchi, J.-D. Chiche, N. Weiler, C. S. Uiterwaal, and A. J. van Vught, "High frequency oscillatory ventilation compared with conventional mechanical ventilation in adult respiratory distress syndrome: a randomized controlled trial [ISRCTN24242669]," *Crit. Care* **9**(4), R430–R439 (2005).
  24. N. Uribe-Patarroyo and B. E. Bouma, "Rotational distortion correction in endoscopic optical coherence tomography based on speckle decorrelation," *Opt. Lett.* **40**(23), 5518–5521 (2015).
  25. Cambridge University Engineering Department, *Materials Data Book* (Cambridge, 2003).
  26. J. B. Lissauskas and M. Siebes, "Investigation of plaque biomechanics from intravascular ultrasound images using finite element modeling," in *IEEE Engineering in Medicine and Biology Society* (IEEE, 1997), Vol. 2, pp. 887–888.
  27. P. R. Herz, Y. Chen, A. D. Aguirre, K. Schneider, P. Hsiung, J. G. Fujimoto, K. Madden, J. Schmitt, J. Goodnow, and C. Petersen, "Micromotor endoscope catheter for in vivo, ultrahigh-resolution optical coherence tomography," *Opt. Lett.* **29**(19), 2261–2263 (2004).
  28. B. Lau, R. A. McLaughlin, A. Curatolo, R. W. Kirk, D. K. Gerstmann, and D. D. Sampson, "Imaging true 3D endoscopic anatomy by incorporating magnetic tracking with optical coherence tomography: proof-of-principle for airways," *Opt. Express* **18**(26), 27173–27180 (2010).
  29. K. P. Strohl, J. P. Butler, and A. Malhotra, "Mechanical properties of the upper airway," *Compr. Physiol.* **2**(3), 1853–1872 (2012).
  30. R. Arens, J. M. McDonough, A. M. Corbin, N. K. Rubin, M. E. Carroll, A. I. Pack, J. Liu, and J. K. Udupa, "Upper airway size analysis by magnetic resonance imaging of children with obstructive sleep apnea syndrome," *Am. J. Respir. Crit. Care Med.* **167**(1), 65–70 (2003).

## 1. Introduction

Obstructive airway disorders (OADs) lead to increased health risks, impaired quality of life, and life-threatening respiratory failure. Obstructive sleep apnea (OSA) is highly prevalent among adults [1] and is characterized by dynamic collapse that reduces airflow [2]. Tracheobronchomalacia (TBM) is another common disorder, in which the stiffness of the tracheal and bronchial walls are reduced [3]. It is hypothesized that dynamic collapse tends to occur at locations within the airway where the tissues are highly compliant. However, there are few available methods to quantify airway compliance (defined as the change in luminal

volume per unit change in transmural pressure). While pulmonary function tests are commonly used, they measure overall lung compliance, which is not specific to the large airways [4]. Quantitative imaging techniques that measure local biomechanical tissue properties could therefore be of great aid in diagnosis and treatment monitoring of these disorders. A straightforward and localized parameter that can be obtained from imaging is the cross-sectional compliance (CC), *i.e.*, the change in luminal cross-sectional area (CSA) per unit change in transmural pressure. CC corresponds to the circumferentially-averaged compliance of the local tissue, under the assumption that the length of the airway (or axial strain) does not change significantly during respiration. For accurate quantification of CC in the airway, the imaging technique should have the ability to accurately measure both CSA and transmural pressure simultaneously during breathing, while posing minimal health risk. In this way, imaging can aid in 1) identifying regions with high compliance that may be susceptible to collapse in patients suffering from OADs [5], 2) providing formative new data to supplement what little is currently known about the size and heterogeneity of compliance in OADs, leading to new hypotheses and stratification of severity of disease for multiple OADs, 3) providing new insight into the mechanics of dynamic collapse by informing mechanical models with unprecedented accuracy in quantifying pressure and lumen geometry simultaneously and in real-time. Toward this end, here we present measurements of CC using a swept-source anatomic optical coherence tomography (SSaOCT) system, which offers high-resolution and high-speed imaging deployed via an endoscopic catheter, used in conjunction with a ventilator or a bag valve mask (BVM) for pressure control.

The current gold standard for airway imaging is video endoscopy, which can provide direct visualization of the airway tract via a bronchoscope. While video bronchoscopic images can be analyzed to extract dynamic CSA data and measure CC [6], CSA measurements require manual interpretation and are semi-quantitative at best. Imaging techniques like CT and MRI are commonly used in diagnosis and monitoring of airway obstructive disorders and provide quantitative data. As such, they have also been used in research studies for measuring airway CC [6,7]. However, ionizing radiation from CT and long scan times in both MRI and CT, the former of which, for children and infants, may require anesthesia or sedation [5,8], make these modalities sub-optimal for diagnosis or monitoring. In addition, performing CT or MRI during surgery can be challenging, and are therefore not the best solution for routine intra-operative guidance.

Optical coherence tomography (OCT) is an attractive alternative for airway imaging, which uses near-infrared (NIR) light with low-coherence interferometry to achieve precise axial sectioning in highly scattering media [9]. Compared with CT and MRI, it provides higher resolution, faster scan rates, and poses no health risks beyond that of standard endoscopy. The high resolution afforded by OCT enables detailed assessment of tissue deformation under load, which can be used to quantify tissue biomechanical properties, also known as optical coherence elastography (OCE) [10]. However, conventional OCT/OCE is typically designed for depth scans of only a few millimeters, due to the limited depth penetration of light into tissues. For imaging of the upper and central airway lumen, which can have a diameter exceeding 10 mm, anatomic OCT (aOCT) for capturing targets at long ranges is required [11]. While early upper/central airway endoscopic studies employed time-domain aOCT, the development of swept source aOCT (SSaOCT) has enabled airway imaging with higher speed [12] due to the signal-to-noise ratio (SNR) advantage of swept-source OCT in comparison to time-domain OCT [13].

The exceedingly high resolution afforded by aOCT has enabled many new applications for studying and treating airway obstructive disorders. For example, aOCT has been used to assess geometric differences between individuals with and without OSA to identify geometric predictors of the disease [14]. Computational fluid dynamics using aOCT-derived luminal geometries has provided insight into how small changes in shape can lead to significant changes in intraluminal pressure that characterize OSA [15]. For assessing tissue

biomechanical properties, aOCT has been applied to quantify CSA vs. pressure at the velo-, oro-, and hypopharynx while investigating OSA pathophysiology [16] and to study regional changes in central airway CC in individuals suffering from asthma, COPD, and bronchiectasis [17]. Recently, SSaOCT was used to quantify luminal geometry changes intraoperatively before and after laryngeal microsurgery for treating subglottic stenosis [18].

Here we employ an SSaOCT system that has previously been validated to provide accurate tracheal CSA in comparison to micro-CT scans [19]. Taking this one step further, here we employ the same system to assess the validity of CC measurements obtained by collecting CSA and pressure simultaneously. This is accomplished by comparing results of simulations and a model of elastic deformation with experimental data of an elastic phantom and *ex vivo* tracheas. The SSaOCT system utilizes a fiber-based catheter probe that is deployed through a standard flexible bronchoscope to simulate the clinical imaging scenario. The bronchoscope is a familiar tool for clinicians where the endoscopic video provides real-time guidance for probe positioning within the area of interest. Pressure was controlled during imaging using a ventilator in the phantom study, and a BVM for *ex vivo* tracheas. However, for all proximally-scanned fiber-optic OCT systems, there is non-uniform rotational distortion (NURD) due to bending and friction of the catheter [20,21]. To understand the impact of NURD on compliance measurements, we performed simulations to investigate to what degree NURD affects the accuracy of CC measurements, and explore the impact of NURD experimentally using a notched tube. Subsequently, we demonstrate the reliability of CC measurements obtained with our system by comparing a model of elastic deformation with imaging of a deformable phantom. Finally, we demonstrate CC measurements in the *ex vivo* tracheas to assess its elastic properties. Ultimately, this effort provides important insight into the potential accuracy of aOCT systems for measuring compliance of the airway, providing needed guidance necessary to fully adapt this technique into the clinical setting for diagnosis and treatment of airway obstructive disorders.

## 2. Methods

### 2.1 aOCT system and image acquisition

Our anatomic OCT system (Fig. 1) is based on a wavelength-swept laser source (HSL-2100-LC Santec Inc.), which provides a NIR light beam at a 5 kHz sweep rate. The center wavelength of the beam is 1310 nm, and the sweeping range is 30 nm. The long coherence length of 17.5 mm enables a large depth range for anatomical imaging of the upper airway. The light beam is directed into a Mach-Zehnder interferometer, and the back-scattered signal is processed to retrieve the depth information. The fiber catheter, manufactured by Physical Sciences Inc., consists of an SMF-28 fiber with an angle-ground ball lens at its tip to produce a side looking beam with a 15° forward tilt. The fiber is enclosed in a flexible Nitinol tubing that serves as the driveshaft and placed in a sealed protective sheath (Fig. 1, right inset). The catheter is 170 cm long with an outer diameter of 0.86 mm (including the sheath). The driveshaft is connected to a scanning engine (Physical Sciences Inc.) that simultaneously rotates and translates the catheter to achieve a helical pull-back scan. The catheter is introduced into the specimen via the side-port of a flexible pediatric bronchoscope (11003BC, Karl Storz GmbH & Co.), which provides white light video images that serve for real-time guidance of the procedure.

As described previously [21], the aOCT system has an axial resolution of 25.7  $\mu\text{m}$ , and a transverse resolution of 100  $\mu\text{m}$  at an imaging distance of 2.7 mm, enlarging to 400  $\mu\text{m}$  at a distance of 12 mm. The output power of the laser source is 16.5 mW, and the output power at the end of the catheter is 4~6 mW. The signal-to-noise ratio (SNR) of the system is 98 dB at 2 mm imaging depth, decreasing to 81 dB at 11 mm.

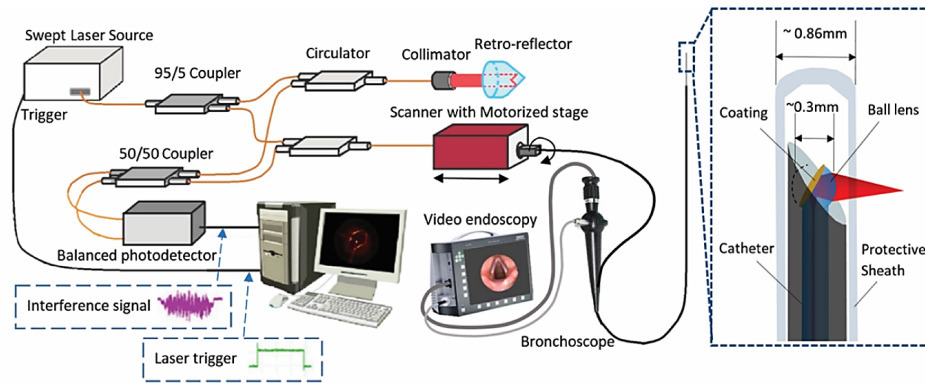


Fig. 1. Diagram of the aOCT system for upper airway endoscopy, and ball lens fiber-optic catheter.

For each aOCT scan, the bronchoscope is positioned inside the target and the catheter is positioned so that it extends  $\sim 28$  mm from the bronchoscope tip. Video endoscopy is used to optimize the position of the catheter nearer the center of the lumen to minimize the impact of NURD (see section 3.2). A helical scan with  $\sim 25$  mm pull-back distance is then performed on the target. The pull-back speed of the scanner is set to 6 mm/s, with a rotation rate of 20Hz, providing 20 frames/s of the target luminal cross-section at a pitch of  $300 \mu\text{m}$ . A continuous OCT image of the object is captured, and subsequently, the luminal surface is segmented using a semi-automated segmentation algorithm similar to our previous method [19]. For CC measurement, CSA is calculated by integrating the segmented surface radii overall A-lines within each rotation. For visualization, this helical 2D data (both the OCT imaging data and the segmented surface data) is resampled into 3D Cartesian space with sampling sizes of 0.05 mm and 0.1 mm within the slice plane and between slices, respectively. Representative slices from the 3D Cartesian imaging data, and reconstructions from the 3D Cartesian segmentation data, are displayed in figures below. All of the above methods account for the tilt of the laser beam as it emerges from the catheter tip, which is directed  $15^\circ$  forward from perpendicular.

## 2.2 Model of compliance for a tube phantom

Ultimately, compliance is associated with the underlying elastic properties of the airway wall. To show that aOCT-derived measurements of CC are well-behaved in a more simplified elastic system, here we employ a phantom comprised of a tube-shaped Latex balloon which is assumed to be cylindrical, linear elastic and homogeneous. We model this phantom using expressions of stress for a thick-walled tube [22] to develop a general expression for the CC as a function of the inner and outer radii of the tube ( $a$  and  $b$ , respectively), the inner and outer pressures applied to the tube ( $p_i$  and  $p_o$ , respectively), and the Young's modulus and Poisson's ratio of the tube material ( $E$  and  $\nu$ , respectively). Since the tube is closed at the distal end, it develops non-negligible axial stress ( $\sigma_z$ ), in addition to radial ( $\sigma_r$ ) and circumferential ( $\sigma_\theta$ ) stresses. The stresses in this geometry under these boundary conditions are:

$$\sigma_r = \frac{A}{r^2} + B, \quad \sigma_\theta = -\frac{A}{r^2} + B, \quad \sigma_z = B, \quad (1)$$

where  $r$  is the radius at which the stress is calculated, and

$$A = \frac{a^2 b^2 (p_o - p_i)}{b^2 - a^2}, \quad B = \frac{p_i a^2 - p_o b^2}{b^2 - a^2}. \quad (2)$$

The tangential strain can then be determined by:

$$\varepsilon_{\theta} = \frac{1}{E}(\sigma_{\theta} - \nu(\sigma_r + \sigma_z)). \quad (3)$$

This component of strain is related to the radial and circumferential components of displacement,  $u$  and  $v$  respectively, as:

$$\varepsilon_{\theta} = \frac{u}{r} + \frac{\partial v}{r \partial \theta}. \quad (4)$$

Because the system is axisymmetric, there is no angular dependence and the radial displacement may be written as  $u = r\varepsilon_{\theta}$ .

In our imaging scenario, the change in the luminal area is measured between a state of no pressure ( $\Delta p = p_i - p_o = 0$ ), and a state of overpressure ( $\Delta p > 0$ ). To model this change in area, we first determine the change in the luminal radius,  $\Delta a$ , by computing the difference in  $u$  between the two pressure values, and evaluating it at the inner surface of the tube ( $r = a$ ):

$$\Delta a = a(\varepsilon_{\theta}(r = a, p_i = p_o + \Delta p) - \varepsilon_{\theta}(r = a, p_i = p_o)). \quad (5)$$

Using the expressions above,  $\Delta a$  is proportional to the overpressure,  $\Delta p$ , as:

$$\Delta a = a \cdot \Delta p \cdot x, \quad x = \frac{1}{E} \frac{b^2(1+\nu) + a^2(1-2\nu)}{(b^2 - a^2)}. \quad (6)$$

The cross-sectional area may be expressed as:

$$CSA = \pi(a + \Delta a)^2 = \pi a^2(1 + \Delta p \cdot x)^2, \quad (7)$$

Finally, CC can be determined by taking the partial derivative of the area with respect to the overpressure:

$$CC = \frac{\partial CSA}{\partial(\Delta p)} = 2\pi a^2(x + \Delta p \cdot x^2) \approx 2\pi a^2 x. \quad (8)$$

Interestingly, CC is not technically a constant, as the second term in Eq. (8) shows an increasing trend with  $\Delta p$ . In practice, we observe no statistically significant nonlinearity in CSA with  $\Delta p$ , and thus we computed the theoretical CC using the linear approximation of Eq. (8), where CC is a constant that is a function of the Young's modulus, Poisson's ratio, and inner and outer radii of the tube. Because the phantom collapses in the absence of overpressure, we estimated the inner radius  $a$  by extrapolating the CSA vs. pressure curve to zero overpressure, then estimated the outer radius  $b$  by adding the known thickness to the value of  $a$ . In this way, the theoretical CC (using values of  $E$  and  $\nu$  given below) was computed for specific positions along the phantom for comparison to the experimental CC.

### 2.3 Compliance measurement protocol

For compliance measurements of the tube phantom, a ventilator (SERVO 900C, Siemens-Elementa AB) was set to provide controlled pressures to the specimen. The pressure signal from the inspiration pressure transducer on the ventilator was digitized at 1.67 kHz to provide real-time pressure data during the aOCT scans (which tended to vary by 2-3 cmH<sub>2</sub>O), and was synchronized with aOCT data acquisition through the laser trigger. To inflate the phantom, a swivel adapter was used to connect the phantom, the bronchoscope and the ventilator (Fig. 2). A diaphragm on the adapter allowed for the bronchoscope to be inserted and positioned within the sample with minimal air leakage. For the tracheas, an endotracheal tube with an inflatable cuff was introduced after the adapter to prevent air leakage from the proximal end of the tracheas. Due to the unpreventable air leakage, the feedback signal from the ventilator

led to large deviation of the output pressure for *ex vivo* trachea compliance measurement. To circumvent this problem, we used a bag valve mask (BVM) to manually maintain constant pressure while reading the built-in pressure gauge. We estimate that the deviation of the pressure applied in this manner was less than  $\pm 10\%$ .

Phantom imaging was performed with inspiratory pressures set to 0, 5, 10, 15, 20, 25, 30, 35 and 40 cm H<sub>2</sub>O, and tracheal imaging was performed with pressure at the BVM maintained at 0, 10, 20, 30, 40 cmH<sub>2</sub>O. The pressure of up to 40cmH<sub>2</sub>O in CC measurements is only used here for verifying the validity of our linear approximation [23], and would not be recommended for clinical imaging. At each pressure value, aOCT scans were collected and segmented in order to tabulate CSA at each longitudinal position. For phantom experiments, the real-time pressure measured at each longitudinal position was also tabulated for each pressure setting of the ventilator. The CSA versus pressure was subsequently analyzed by linear regression, where the slope of the CSA-versus pressure curve was used to determine CC at each position (*i.e.*, for each slice in the reconstruction). The data obtained at 0 pressure was omitted from the regression analysis, due to the collapse of the sample with the absence of overpressure.

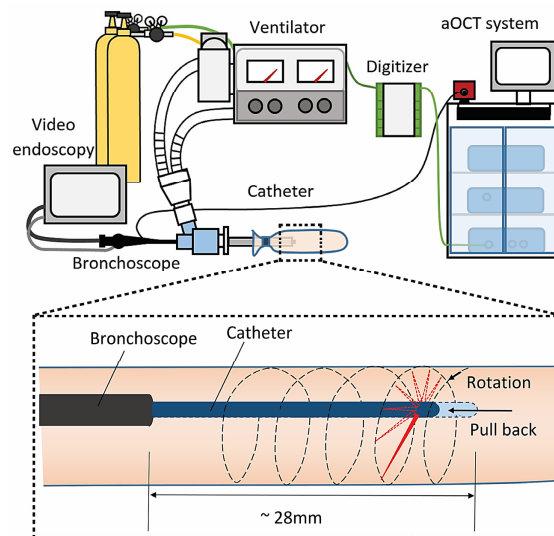


Fig. 2. Diagram of the compliance measurement setup with the SSaOCT system and ventilator for phantom experiments. The ventilator is connected to the system to provide positive inspiratory pressure into the tube phantom, and the pressure value is recorded by the digitizer. The helical scan of the catheter inside the tube is enlarged to show the detailed pattern.

## 2.4 Pig trachea

The tracheas ( $n = 2$ ) were excised from freshly euthanized pigs, and the bronchial openings of the tracheas were sutured to prevent air leakage during the experiment. Independent aOCT scans were performed at different anatomical positions in tracheas to verify the repeatability of our measurement protocol. The lumen of the trachea was not visible in certain scans, particularly at large pressures or with the catheter being off-center; such scans were excluded as it was not possible to segment the airway lumen due to roll off of the OCT signal at larger radial distances.

## 3. Results and discussion

### 3.1 Geometric validation

In previous work, we assessed the accuracy of CSA measurements in static objects including cylindrical tubes and excised tracheas, which demonstrated that CSA captured by the

SSaOCT system is consistent with CSA obtained by manual caliper measurements or by CT measurements [19]. Here, we employed a customized notched tube to specifically challenge the ability of SSaOCT to accurately pinpoint abnormalities, and to investigate the impact of NURD. Figure 3(a) shows a 3D diagram of the notched tube. The inner diameter of the tube was 8 mm, which was similar to an adult human trachea. There were ring structures every 5 mm in the axial direction, and four 1 mm-wide notches symmetrically distributed inside the tube along the length of 40 mm. One of the rings had a different depth and interval spacing from the others.

Figure 3(b) shows the 3D reconstruction corresponding to an aOCT scan of the notched tube. All of the rings and notches are clearly seen. This demonstrates that the system can detect both circumferential and longitudinal features. The different position of the special ring in the tube was also positioned correctly according to the aOCT scan. In Fig. 3(c), the comparison between the luminal surface segmented from the aOCT scan and the real structure of the tube are shown along both the longitudinal and circumferential directions. The longitudinal comparison shows that aOCT captures the correct position and depth of all notches and abnormalities. In the circumferential comparison, while aOCT reveals the main structure of the tube with four notches, the positions of two of the notches are at different angles than the real structure of the tube. This is an indication of NURD, where the changing rotation rate of the fiber-optic catheter causes a misalignment of the expected angle of each A-scan with the true angular position of the fiber. The presence of NURD arises from several factors that affect the friction between the protective sheath and catheter [24]. The notched tube phantom is helpful for detecting NURD and assessing techniques used to minimize it. Below, we investigate the potential impacts of NURD on CC measurements of the airway.

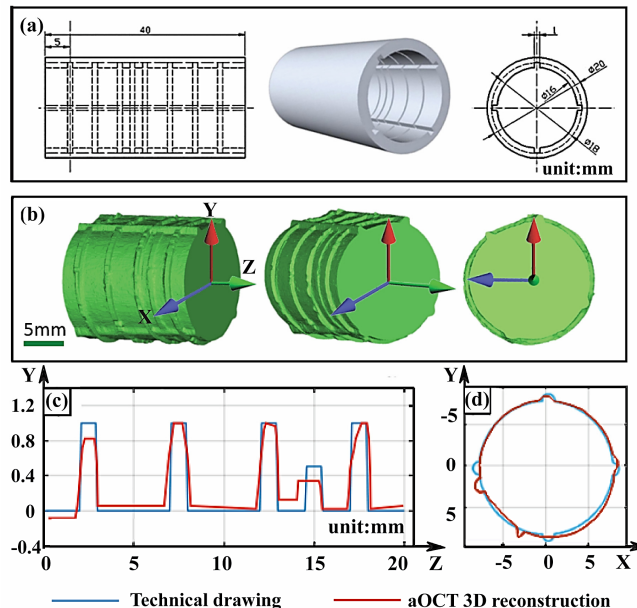


Fig. 3. Notched tube 3D model and its corresponding aOCT 3D reconstruction. (a) 3D model of the notched tube; (b) aOCT 3D reconstruction from different perspectives; (c) and (d) plot of luminal surfaces comparing the aOCT data (red) with the surface from the design drawing (blue); in (d), NURD is apparent as a mis-alignment of the aOCT notches.

### 3.2 NURD simulation and analysis

NURD is caused by time-varying friction between the catheter and the sheath which leads to deviations in rotation rate at the tip of the catheter. This kind of distortion has been observed in all proximally-scanned endoscopic OCT systems. It can lead to inaccurate CSA

measurements and thus may influence the accuracy of CC calculations. To quantify the impact of NURD on CC measurements, here we simulate the influence of NURD on imaging of a circular cross-section, and compute the resulting error in the estimate of CSA and CC.

For simplicity, a two-step function of rotation rate is used to simulate the NURD (as shown in Fig. 4(a)). Then, given the geometry presented in Fig. 4(b), there are four independent parameters that affect the observed image distortions. These factors include: the off-center fraction ( $l_0/a$ ), the impeded rotation fraction ( $\omega_s/\omega_0$ ), the distortion fraction ( $\kappa$ ), and the initial angle ( $\theta_0$ ) of the slow sweep rate. Simulations were carried out for a range of  $l_0/a$ ,  $\omega_s/\omega_0$  and  $\theta_0$  values, as they are the main sources of NURD that control the distortion pattern.

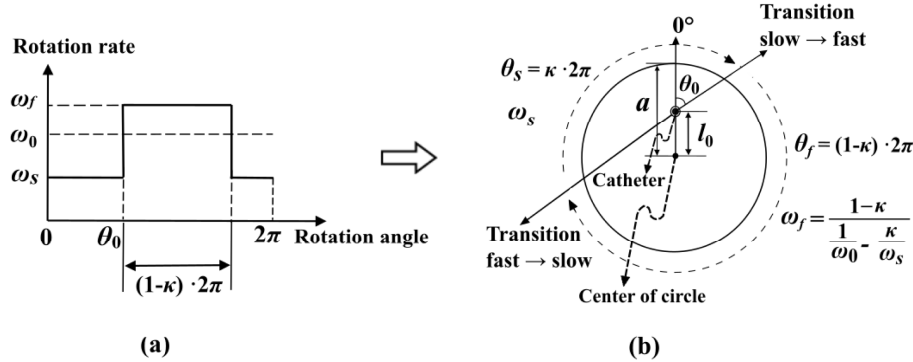


Fig. 4. NURD simulation model. (a) Two-step function of rotation rate with average rotation rate  $\omega_0$  (the rotation rate given by the scanner), slow and fast rotation rates  $\omega_s$  and  $\omega_f$ , respectively, and degree of distortion  $\kappa$  indicating the fraction of the sweep at  $\omega_s$ ; (b) Geometry of catheter position (offset of  $l_0$  from the center of the circular lumen with radius  $a$ ), and catheter sweep angle (initiating a rotation rate of  $\omega_s$  at angle  $\theta_0$  relative to the offset); as the rotation waveform is assumed to be periodic, there are analytical relationships between these parameters.

To simulate CC measurements, the geometry of the cross-section with and without NURD was computed at an initial overpressure of  $\Delta p_0 = 10$  cmH<sub>2</sub>O and a final overpressure of  $\Delta p_f = 30$  cmH<sub>2</sub>O assuming a radius at zero pressure of  $a = 6.5$  mm, and an increase in  $a$  with pressure assuming a CC of 1 mm<sup>2</sup>/cmH<sub>2</sub>O. The corresponding absolute value of the deviation of the CSA ( $\delta_{CSA}$ ) between simulated scans with and without NURD was computed at  $\Delta p_f$ , and the resulting CC ( $\delta_{CC}$ ) was computed according to  $(CSA(\Delta p_f) - CSA(\Delta p_0))/(\Delta p_f - \Delta p_0)$ . The other simulation parameters were set to  $\omega_0 = 20$  Hz and  $\kappa = 0.5$ , which are representative of the phantom experimental conditions, and are used for all of the following simulations.

The results are summarized in the plots in Fig. 5. While NURD does produce quantifiable errors in CSA and CC measurement, the error varies widely with different simulation parameters. In each simulation, only one parameter was varied, while the rest were held constant. In Fig. 5(a), as  $l_0/a$  is varied from 0 to 1 (corresponding to the catheter position varying from the center to touching the wall), there is a positive correlation between both the CSA and CC error and  $l_0/a$ . The CSA error increased from 0 to 2.39% and CC error from 0 to 1.15%. In Fig. 5(b), as the rotation rate  $\omega_s/\omega_0$  is varied from 1 to 0.75 (corresponding to varying from a perfectly uniform rotation rate to a heavily modulated rotation rate), a similar trend is observed in CSA and CC error, which increased from 0 to 6.98% and 0 to 4.23%, respectively. As a point of comparison, using the notched tube data shown in Fig. 3(d), we estimate the ratio of the slowest rotation rate to the average rotation rate,  $\omega_s/\omega_0$ , to be 0.82 in that experiment. While these trends are consistent with what one might intuitively expect, what is interesting to note is that in both cases, the fractional errors in CC are smaller than that of CSA. This can be understood by the CC calculation itself: because CC represents a difference in CSA at two different pressures, even though the overall CSA estimate may be

error-prone, the same geometric distortions are typically observed at both the starting and ending pressures, which results in a partial cancellation as the difference in CSA is computed.

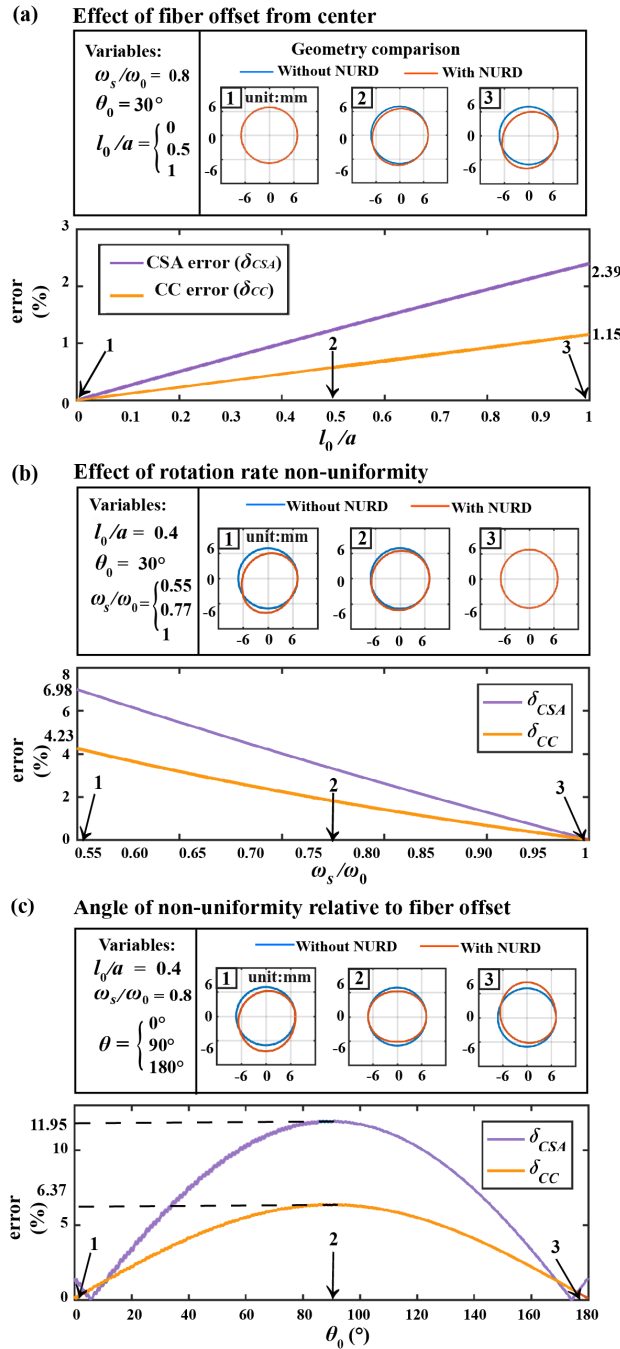


Fig. 5. NURD simulations showing reconstructed circular cross-section geometries at  $p = 30\text{cmH}_2\text{O}$  and corresponding CSA and CC error ( $\delta_{CSA}$ ,  $\delta_{CC}$ ) measurements; in each case, one parameter is varied while the rest remain constant. For each parameter, the comparisons of geometries with and without NURD ( $A_0$ ,  $A_{NURD}$ ) are shown for three conditions corresponding to the positions indicated on the plots of CSA and CC errors.

Surprisingly, the CSA and CC error was highly dependent on the starting angle  $\theta_0$  of the 2-step rotation rate function relative to the catheter displacement (Fig. 5(c)). The CSA error reached up to 11.95% in the worst case scenario ( $\theta_0 = 90^\circ$ ), with a corresponding CC error of 6.37%, while the angle-averaged errors were 7.73% and 3.92%, respectively, for CSA and CC. The errors peak at  $90^\circ$  because this angle corresponds to the slow portion of the sweep occurring when the aOCT beam path is shortest (closest to the wall) and the fast portion when the path is longest, (Fig. 4(b)), thus spending more time with shorter paths and biasing the CSA estimate strongly negative. However, this finding is unique to our choice of a 2-step function with  $\kappa = 0.5$ , and represents a worst-case scenario unlikely to occur in an imaging experiment.

Consistency of distortion throughout each set of scans was observed in the experiments, indicating that within a short scan time, NURD patterns was similar as long as no external disturbance or relative motion was imposed on the catheter or the bronchoscope. These findings suggest some practical steps to reduce the impact of NURD. The use of the notched tube phantom can be used to quantify NURD and test experimental strategies to reduce variable friction in the tubing. However, even if NURD is minimal in a controlled setting, NURD may become exaggerated during a clinical procedure due to bending of the catheter as it is positioned in the airway. Recognizing the presence of NURD by the characteristic kinked features in the luminal geometry, as shown in Fig. 5, can prompt the practitioner to reposition the catheter closer to the lumen center to reduce  $l_0/a$  and reduce the subsequent CC error.

### 3.3 Compliance measurement

#### 3.3.1 Compliance of an elastic tube

In order to verify that aOCT measurements of CSA expansion are consistent with elasticity theory, we employed a tube-like balloon (approximated as a cylinder with a closed end) as a simplified airway phantom to compare with predictions from the elastic model above. The phantom has a wall thickness of  $0.27 \pm 0.01$  mm and inner radius at zero pressure of  $\sim 7$  mm. The phantom is composed of synthetic latex, of which the main component is natural rubber; natural rubber has a reported Young's modulus between 1.5 and 2.5 MPa [25] and Poisson's ratio of 0.49 [26]. If we assume that the balloon's elastic properties are determined by that of natural rubber, the corresponding CC of the balloon should be from 0.34 to 0.57  $\text{mm}^2/\text{cmH}_2\text{O}$ . Considering the existence of other additives to the latex material, the true CC might be expected to be different from this range. We note that it is challenging to construct a phantom that offers a compliance sufficiently large (or, conversely, elasticity and thickness sufficiently small) to mimic that of a trachea. While the latex balloon has undesirable uncertainty in the elastic properties depending on the exact manufacturing conditions, it offered a good compromise for obtaining sufficiently large compliance to test our system in a realistic imaging scenario.

SSaOCT scans at varying pressures were obtained to measure the compliance of the phantom; while this procedure was performed three times, here we present results from the data set exhibiting the most constant CSA across the length of the tube. Figure 6(a) shows representative 2D slices of the phantom at various pressures, where it is effectively collapsed at zero pressure, and expands with increasing pressure. The non-circular geometry also suggests the presence of NURD, as the actual cross-sectional shape of the tube above 0 pressure is largely circular. As mentioned above, NURD changes with the variation of  $l_0/a$ , and during pressure increases, the relative position of the catheter and the phantom can change, resulting in a changing NURD pattern that is subtly seen in Fig. 6(a).

Figure 6(b) shows representative examples of the linear regression used to compute CC at several positions along the tube axis. Raw data showing the CSA across the entire length of the phantom at each pressure is plotted in Fig. 6(c), and the corresponding CC is plotted in Fig. 6(d). The analysis indicates that the phantom has a CC ranging from 0.54 to 0.69

$\text{mm}^2/\text{cmH}_2\text{O}$ , which is slightly larger than that expected of pure, natural rubber. Using the elastic model (Eq. (6) and 8), the derived Young's modulus of the phantom is from 0.95 to 1.27 MPa, which is within a reasonable range due to the production processes of balloons. Importantly, the average value of  $R^2$  from the regression fitting over the entire length of the tube was  $0.998 \pm 0.001$  (mean  $\pm$  std.), indicating the linearity of the aOCT measurement of the phantom's expansion under pressure, consistent with the elastic model. The corresponding standard error of CC, shown as error bars in (d), was  $\pm 0.02 \text{ mm}^2/\text{cmH}_2\text{O}$  on average, or approximately  $\pm 2.5\%$ .

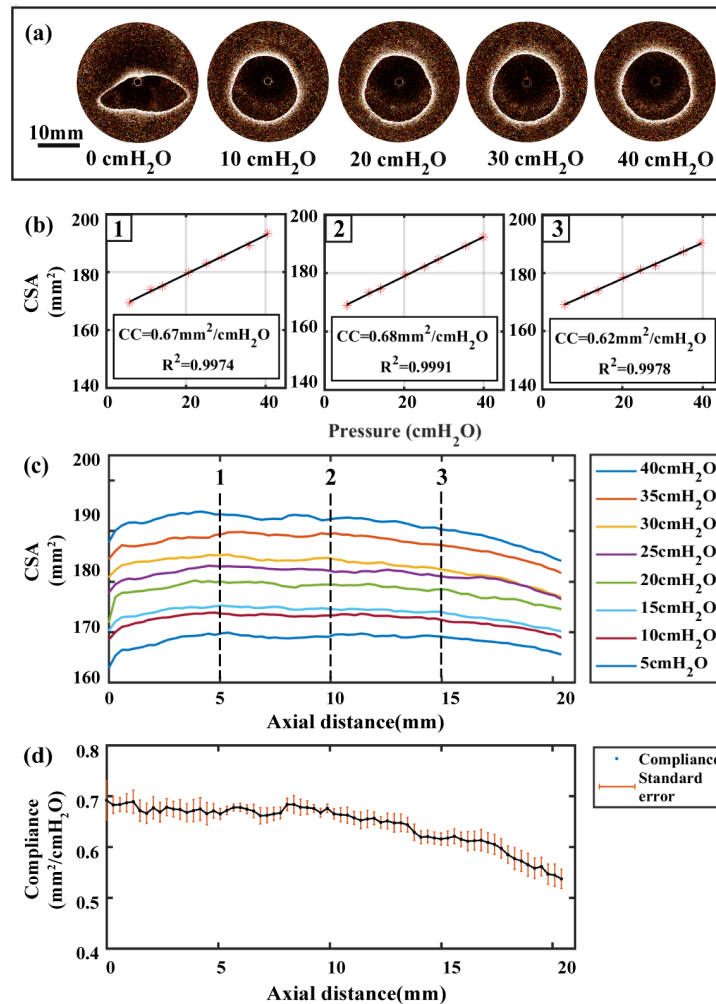


Fig. 6. aOCT imaging and compliance measurement of a tube phantom. (a) Cross-section deformation under different pressures at a single axial position; (b) Linear regression analysis used to determine CC at positions 1, 2 and 3; (c) CSA change under different pressures across the entire aOCT scan, with indication of positions 1, 2 and 3; (d) Corresponding CC with error bars determined from the regression analysis standard error.

### 3.3.2 Compliance of ex vivo tracheas

aOCT scans were performed on porcine tracheas to investigate the ability to measure CC of airway tissues. Imaging data from Trachea 1 at position A (denoted  $A_1$ ) is shown in Fig. 7, and the CC obtained from all other scans are summarized in Table 1. The dilation of the tracheal lumen of  $A_1$  with increasing pressure is evident in the 2D slices and 3D

reconstructions from the aOCT data in Fig. 7(a) and 7(b). Plots of CSA as a function of pressure across the length of the trachea, and the corresponding calculated CC, are shown in Fig. 7(c) and 7(d), respectively. Based on the calculations, the CC varies from 0.98 to 1.37  $\text{mm}^2/\text{cmH}_2\text{O}$  across the length of the trachea. This variation suggests that portions of the trachea might be more compliant than the rest, as relevant to the ultimate goal of identifying compliant regions of the airway susceptible to collapse.

Importantly, for scan  $A_1$ , the  $R^2$  of linear regression across the length of the trachea were all  $>0.98$ , with a mean  $R^2$  of  $0.989 \pm 0.003$ . This demonstrates that the tracheal tissue is highly linearly elastic over the physiological range of luminal pressure, which is favorable for obtaining stable measurements of CC. The standard error of CC (error bars in the plots) is  $\pm 0.13 \text{ mm}^2/\text{cmH}_2\text{O}$ , corresponding to  $\pm 10.4\%$ .

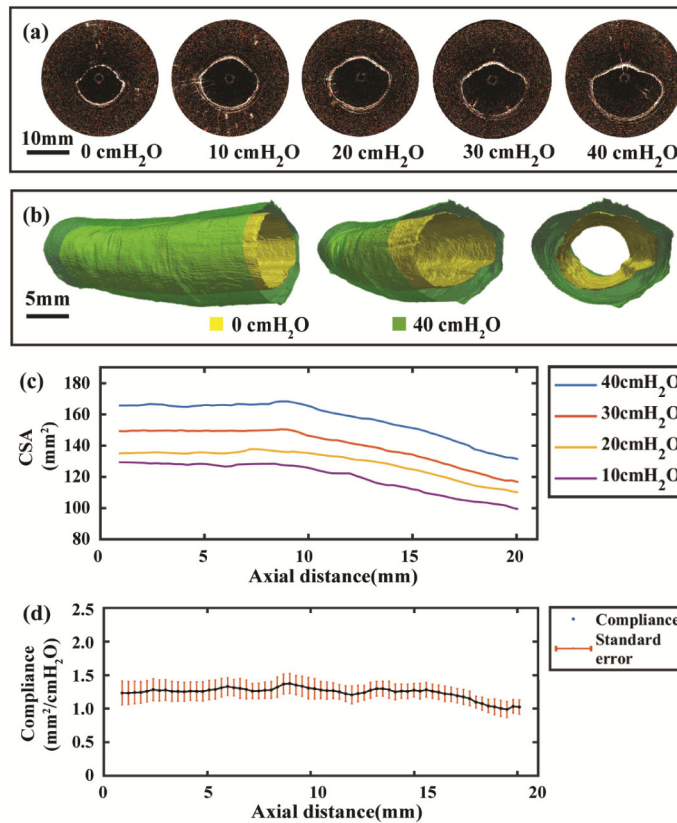


Fig. 7. aOCT imaging and compliance measurement of one of the *ex vivo* porcine tracheas. (a) Representative 2D slices under different applied pressures; (b) Comparison of 3D aOCT reconstructions at 0  $\text{cmH}_2\text{O}$  and 40  $\text{cmH}_2\text{O}$ ; (c) Plots of CSA under different pressures versus distance; (d) Corresponding CC versus distance with standard error as the error bar.

Across all 3 aOCT scans obtained from 2 tracheas (Table 1), the compliance values obtained ranged from 0.63 to 1.52  $\text{mm}^2/\text{cmH}_2\text{O}$ . The average  $R^2$  of all scans is 0.98, suggesting that the tracheal tissues exhibited linear elastic behavior over the physiological pressures used.

Table 1. Compliance results from porcine trachea *ex vivo* experiment

Position	Trachea 1		Trachea 2
	A <sub>1</sub>	B <sub>1</sub>	A <sub>2</sub>
CC (mm <sup>2</sup> /cmH <sub>2</sub> O)	0.98-1.37	0.64-0.88	0.63-1.52
$R^2$	0.989 ±	0.977 ± 0.005	0.964 ± 0.034
Standard error of CC (mm <sup>2</sup> /cmH <sub>2</sub> O)	± 0.13	± 0.11	± 0.11

Compared to the phantom, the CC measurement at a given position of the trachea exhibited a larger standard deviation with typically  $\pm 12\%$  (*i.e.*, the  $R^2$  values were typically less than that for the phantom). Several possible factors could lead to this effect. While NURD contributes to the error in both the phantom and trachea experiments, as tracheas are more curved compared to tube phantom, unpreventable side motion of the trachea during pressure increases causes larger  $l_0/a$  deviation in the trachea, which may increase the error due to NURD. Furthermore, axial strain during pressurization can cause co-registration error of aOCT images, *i.e.*, different regions of tissue with different CSAs can displace into/out of the aOCT image plane, which can cause further error in the CC estimate. While axial stretching of the tracheas was observed in our experiments, we expect that this effect may be partially mitigated *in vivo* due to anchoring of the airway wall. Also, unlike phantom experiments where pressure was recorded in real-time using a sensor, the need to manually maintain and read a constant pressure from the BVM gauge in trachea experiments may produce greater error in the pressure.

#### 4. Summary and conclusion

OCT affords high-resolution imaging of the deformation of upper and central airways under varying pressure, which enables CC measurements of the airway. This may have relevance for understanding airway obstructive disorders. Here we evaluated the linearity and precision of a bronchoscope-deployed SSaOCT system for quantifying CC using modeling, phantoms and *ex vivo* porcine airways under controlled ventilation.

We demonstrated how imaging of a machined tube with notches regularly spaced around the circumference can identify the presence of NURD. We then modeled the impact of NURD on aOCT data, showing how it leads to telltale distortions in the obtained geometry of a circular cross-section. However, while NURD causes error in the estimate of CSA, we found that the resulting error in CC estimation is typically smaller (a reduction of 1- to 2-fold). This reduction in error arises because CC is a measure of the change in CSA with pressure, and thus an offset in CSA has limited impact on CC estimation. This finding thus provides a favorable outlook for quantifying CC in the presence of NURD. At the same time, further research into catheter tube materials and mechanics to reduce friction and/or distribute torque [27], methods for real-time tracking of the rotation rate [28], and/or methods for detecting rotation rate in post-processing [24] can be used to further reduce NURD and its deleterious impacts. Reducing NURD should improve the accuracy of CSA measurements and, as such, lead to a more accurate compliance measurement.

To experimentally assess the ability of our system to quantify CC, we employed a balloon of circular cross-section and well-defined thickness, comparing results to a model for elastic expansion of a closed tube. We found CSA to be highly linear with pressure over the range from 5 – 40 cmH<sub>2</sub>O, with  $R^2 > 0.99$  at all cross-sections. This confirms that the dynamic range of our imaging and pressure measurement systems are appropriate to maintain the linearity of CSA vs. pressure curves measured from deformation of a linearly elastic material (in this case, latex rubber), at values of CC on the same order of magnitude as that found in airways.

Finally, we measured CC on *ex vivo* porcine tracheas under physiologically relevant pressures ranging from 10 – 40 cmH<sub>2</sub>O, with CC values ranging between 0.63 and 1.52 mm<sup>2</sup>/cmH<sub>2</sub>O. Tissues exhibited linearly elastic behavior, with averaged  $R^2 = 0.98$  for all CC

measurements. Interestingly, human upper airway wall compliance measured in the pharynx is somewhat higher than that of the porcine trachea studied here, with CC values being reported as 4.1-9.7 mm<sup>2</sup>/cmH<sub>2</sub>O for normal/healthy adults, and 2.2-12.3 mm<sup>2</sup>/cmH<sub>2</sub>O for patients with OSA [16]. Given this, we might expect that the CSA change in human upper airways will be even larger and easier to measure under the same pressure range, and that the aOCT system described here will be similarly capable of quantifying the deformation and resulting CC in a clinical imaging scenario.

A remaining challenge to clinical translation of this technology is to develop real-time methods to quantify compliance under dynamic pressures typical during respiration. Also, while CC is a useful measure for assessing changes along the length of the airway, methods for assessing more localized changes in tissue elasticity may be needed [16]. In combination with position tracking of the aOCT catheter tip, the exact anatomic position for each data point could be determined to enable elastographic reconstruction, providing clinicians with new insight into airway obstructive disorders. For example, airway elastography maps can potentially be used to locate sites of compliant tissues susceptible to collapse, and aid clinicians in discriminating pathologies in extremely common conditions such as sleep apnea as well as other disease processes. The highly accurate compliance measurements afforded by aOCT can also be used to inform computational fluid dynamics modeling of airflow. The unique ability for aOCT to provide instantaneous, local deformation and pressure data enables quantitatively correct modeling of the airway fluid-structure interaction, which is a prerequisite for prediction of airway collapse. In particular, the delayed response of airway cross section to changes in pressure is essentially a rheometric probe that can be used to extract the local viscoelastic moduli of airway tissue at various pressures. The resulting data can be incorporated into a computational model that then provides individualized prediction of possible airway collapse. Ultimately, the ability to rapidly and accurately measure airway wall compliance using endoscopic aOCT will provide clinicians with a powerful new tool for diagnosis, monitoring, and treatment of patients suffering from airway obstructive disorders.

### Funding

National Institutes of Health, National Heart, Blood, and Lung Institute (R01HL123557, R21HL111968, and R21HL130901) (Oldenburg).

### Acknowledgments

We thank Prof. Julia Kimbell, Department of Otolaryngology, UNC, for aiding with the 3D reconstructions, and Mark Hall, NC Children's Airway Center, for assistance with the ventilator setup and ventilation protocol. We are also thankful to Prof. Sorin Mitran, Department of Mathematics, UNC, for providing expertise in the discussion of aOCT-derived compliance measurement.